

# Effect of oxygen partial pressure and VO<sub>2</sub> content on hexagonal WO<sub>3</sub> thin films synthesized by pulsed laser deposition technique

Ajay Kaushal · Davinder Kaur

Received: 12 July 2010 / Accepted: 2 November 2010 / Published online: 20 November 2010  
© Springer Science+Business Media B.V. 2010

**Abstract** We report on the effect of oxygen partial pressure and vacuum annealing on structural and optical properties of pulsed laser-deposited nanocrystalline WO<sub>3</sub> thin films. XRD results show the hexagonal phase of deposited WO<sub>3</sub> thin films. The crystallite size was observed to increase with increase in oxygen partial pressure. Vacuum annealing changed the transparent as-deposited WO<sub>3</sub> thin film to deep shade of blue color which increases the optical absorption of the film. The origin of this blue color could be due to the presence of oxygen vacancies associated with tungsten ions in lower oxidation states. In addition, the effects of VO<sub>2</sub> content on structural, electrochemical, and optical properties of (WO<sub>3</sub>)<sub>1-x</sub>(VO<sub>2</sub>)<sub>x</sub> nanocomposite thin films have also been systematically investigated. Cyclic voltammogram exhibits a modification with the appearance of an extra cathodic peak for VO<sub>2</sub>–WO<sub>3</sub> thin film electrode with higher VO<sub>2</sub> content ( $x \geq 0.2$ ). Increase of VO<sub>2</sub> content in (WO<sub>3</sub>)<sub>1-x</sub>(VO<sub>2</sub>)<sub>x</sub> films leads to red shift in optical band gap.

**Keywords** WO<sub>3</sub>–VO<sub>2</sub> · Oxygen partial pressure · Pulsed laser deposition · Synthesis · Nanolayers

## Introduction

Tungsten trioxide (WO<sub>3</sub>) as a metal oxide semiconductor has attracted considerable interest because of its vast technological applications in smart windows, gas and humidity sensors, and other optoelectronic devices as reported by Granqvist (1990; 1991). In thin film form, tungsten oxide has found unique application in electrochromic devices because of their excellent voltage-modulated optical properties (Granqvist et al. 2003; Jelle and Hagen 1999). Recently, tungsten oxide thin films have been used as gas sensors, transparent conducting electrodes, photochromic devices, and as a catalyst (Qu and Włodarski 2000; Lee et al. 2000; Robert and Ivan 2004). WO<sub>3</sub> is quite a complicated material with respect to the crystal structure. There are reports on monoclinic (Poirier et al. 2009), orthorhombic (Pecquenard et al. 1998), cubic, triclinic, tetragonal (Walkingshaw et al. 2004), hexagonal WO<sub>3</sub> (Kumagai et al. 1996), and several oxygen-deficient phases, for instance, WO<sub>2.90</sub>, W<sub>18</sub>O<sub>49</sub>, etc. (Pickering and Tilley 1976). Among various crystal structures of WO<sub>3</sub>, hexagonal form of tungsten trioxide (*h*-WO<sub>3</sub>) is of great interest owing to its known tunnel structure which serves as intercalation host to obtain hexagonal tungsten bronzes M<sub>x</sub>WO<sub>3</sub> (M = H<sup>+</sup>, Li<sup>+</sup>, Na<sup>+</sup>, K<sup>+</sup>, etc.). The structure of *h*-WO<sub>3</sub> belongs to the space group P6/mmm in which every six [W-O<sub>6</sub>] octahedra linked by corner sharing from hexagonal channels oriented along the *c*-axes (Gerand et al. 1979).

A. Kaushal · D. Kaur (✉)  
Department of Physics and Center of Nanotechnology,  
Indian Institute of Technology Roorkee, Roorkee, India  
e-mail: dkaurfph@iitr.ernet.in

Various physical and chemical vapor deposition techniques such as magnetron sputtering (Kaneko et al. 1988), sol-gel (Ozer and Lampert 1998), spray pyrolysis (Reragui et al. 2001), electron beam evaporation (Sivakumar et al. 2007), and pulsed laser deposition (PLD) (Mitsugi et al. 2003) have been used to deposit single or mixed metal oxide films. The properties of  $\text{WO}_3$  films were found to be influenced by various deposition methods, such as the deposition techniques resulting in different properties of these films in terms of composition, structure, morphology etc. In this study,  $(\text{WO}_3)_{1-x}(\text{VO}_2)_x$  nanocomposite thin films of different  $\text{VO}_2$  contents ranging from  $x = 0.0$  to  $x = 0.4$  have been synthesized by PLD. PLD has been recognized as a promising versatile technique for the deposition of stoichiometric films of mixed metal oxides at high deposition rate (Kaur et al. 2005; Kumar et al. 2006). Takami et al. (2010) have recently reported on W-doped  $\text{VO}_2$  thin films via hard X-ray core-level photoemission spectroscopy. Doping of a transition metal ion, like vanadium, may introduce impurity levels in the band gap of  $\text{WO}_3$  and aid in preventing the recombination of the photo-generated carriers (Ashokkumar and Maruthamuthu 1989) and may also influence the band gap. Moreover, the ionic radius of  $\text{W}^{6+}$  (0.64 Å) are somewhat larger than that of  $\text{V}^{4+}$  (0.63 Å), therefore doping of  $\text{VO}_2$  in  $\text{WO}_3$  thin films may enable vanadium ion to be substituted ( $\text{V} \rightarrow \text{W}$ ) because of structural adjustment. This substitution may lead to variation in various properties of  $\text{WO}_3$  thin films. Therefore,  $\text{WO}_3$  thin films were grown on quartz substrate to investigate the effect of  $\text{VO}_2$  on optical and electrochemical properties of  $\text{WO}_3$  thin films. Rougier et al. 1999, 2001) have reported on electrochemical properties of  $\text{WO}_3$  thin films deposited on  $\text{SnO}_2$ : F-coated glass via PLD. In the experimental system the stability of hydrogen intercalation is slightly difficult to maintain, as it is quite mobile because of its small size (Ingham et al. 2005). Both Hydrogen and Lithium are ions that are too small in size to be able to occupy the small triangular sites between the hexagonal tunnels. We report on  $\text{H}^+$  ion intercalation in hexagonal  $\text{WO}_3$  thin films. To get the desired hexagonal phase of  $\text{WO}_3$  thin films, the oxygen partial pressure ( $P_{\text{O}_2}$ ) was optimized by varying in the range from 10 to 100 mTorr. Fumiaki et al. (2003) explored the effect of oxygen partial pressure on the structure properties of  $\text{WO}_3$  films and have reported that there is no considerable change in grain size with

oxygen partial pressure. Gyorgy et al. (2005) have investigated the effect of ambient gas pressure and substrate temperature on compositional and optical properties of  $\text{WO}_3$  thin films. Hussain et al. (2005) have reported on the influence of high oxygen partial pressure of 100, 200, and 300 mTorr on laser-ablated  $\text{WO}_3$  thin films at 600 °C. They have observed a decrease in grain size with increase in oxygen partial pressure. Despite the numerous scientific investigations, many of the results are conflicting, and additional study remains to be done to elucidate the influence of process parameters on microstructure and physical properties of these films. Therefore, in this study,  $\text{WO}_3$  thin films were grown on quartz substrate using pulsed laser deposition technique and the influence of varying oxygen partial pressure ( $P_{\text{O}_2}$ ) in the range from 10 mTorr to 100 mTorr and post-annealing on  $\text{WO}_3$  thin films has been investigated. In addition, attempts have been made to investigate the effect of  $\text{VO}_2$  on structural, optical, and electrochemical properties of  $\text{WO}_3$  thin films.

## Experimental details

Nanocrystalline  $\text{WO}_3$  thin films were grown on quartz substrate using pulsed laser deposition technique. The excimer laser KrF (Lambda Physik) with wavelength of 248 nm was used for deposition. The pulse repetition rate was kept constant to 10 Hz with fixed laser energy of 350 mJ. Three sets of samples were grown to study the effects of (i) oxygen partial pressure (ii) post-annealing in  $\text{WO}_3$  thin films, and (iii)  $\text{VO}_2$  content in  $(\text{WO}_3)_{1-x}(\text{VO}_2)_x$  films. In the first set,  $\text{WO}_3$  thin films were grown at different  $P_{\text{O}_2}$  of 10, 30, 50, and 100 mTorr. In the second set of samples,  $\text{WO}_3$  thin films were deposited at substrate temperature of 600 °C, and oxygen partial pressure of 30 mTorr were post-annealed in vacuum for 30 min at the same temperature. In the third set of samples,  $(\text{WO}_3)_{1-x}(\text{VO}_2)_x$  thin films of different  $\text{VO}_2$  contents in the range from  $x = 0.0$  to  $x = 0.4$  were synthesized. Various deposition parameters of deposited films are listed in Table 1. The targets were prepared by the conventional solid-state reaction method. High-purity  $\text{WO}_3$  and  $\text{VO}_2$  powders were thoroughly mixed and calcined at 400 °C for 6 h in air. After calcination, the powders were pressed into pellets and sintered at 700 °C for 8 h. The substrates were cleaned sequentially in

acetone, methanol, and de-ionized water before deposition. The target-to-substrate distance was kept at 40 mm. The thickness of the films was measured using surface profiler. The orientation and crystallinity of these films were studied using a Bruker diffractrometer of  $CuK\alpha$  (1.54 Å) radiations in a  $\theta$ – $2\theta$  geometry. The morphology of the outermost surface layer was studied by means of atomic force microscopy in a tapping mode. Optical properties were studied using Cary 5000 UV–VIS/NIR spectrometer in the wavelength range of 200–800 nm.

Electrochemical properties of these films were studied in cyclic voltammetric mode using Bioanalytical System CV-50W voltammetric analyzer. The electrode of the thin films were made by making a contact of the film with a copper strip and then the whole assembly was wrapped with a good quality scotch tape keeping a hole of 3-mm diameter in the tape just above the film to expose that particular area of the film to be in contact with the electrolyte solution. Cyclic Voltammetric (CV) analysis was carried out using Bioanalytical System (BAS, West Lafayette, IN, USA) CV-50W voltammetric analyzer in a single-compartment three-electrode glass cell with the exposed part of deposited samples as working electrode, a platinum wire as counter electrode, and Ag/AgCl electrode as reference (Model MF-2050 RB-5B) electrode. Phosphate buffer solution of 1.0 M concentration and pH value of 7.2 was used as electrolyte. Phosphate buffer solution was prepared in double distilled water as per Christian and Purdy

method (Christian and Purdy 1982). All the experiments were carried out at an ambient temperature.

## Results and discussion

### Effect of oxygen partial pressure on structural and optical properties of $WO_3$ thin films

Figure 1 shows the XRD pattern of  $WO_3$  thin films deposited at different oxygen partial pressure ( $P_{O_2}$ ) ranging from 10 to 100 mTorr. It can be clearly seen from the XRD pattern that the crystallinity of the films increases with increase in oxygen partial pressure. The pattern revealed that the films deposited at low oxygen partial pressure of 10, 30, and 50 mTorr exhibit a dominant (201) diffraction peak corresponding to hexagonal phase of  $WO_3$  (JCPDS card No. 75-2187). However, the film deposited at higher oxygen partial pressure of 100 mTorr shows several X-ray diffraction peaks along (001), (111), (112), (202), (004), (114), (204), and (442) lattice reflection planes corresponding to orthorhombic phase of  $WO_3$  (JCPDS card No. 71-0131) with a preferred oriented growth along (001) plane. Hence, a structural phase transition from hexagonal to more stoichiometric orthorhombic phase has been observed with increase in oxygen partial pressure from 50 to 100 mTorr, which could be a result of the modification in mechanism of thin film growth due to the presence of sufficient oxygen pressure. It has been reported that at higher oxygen pressure,

**Table 1** Various optimized parameters for deposited films

PLD parameters	1st set	2nd set	3rd set
Laser	KrF excimer	KrF excimer	KrF excimer
Laser wavelength	248 nm	248 nm	248 nm
Laser energy	350 mJ	350 mJ	350 mJ
Repetition rate	10 Hz	10 Hz	10 Hz
Target used	$WO_3$	$WO_3$	$(WO_3)_{1-x}(VO_2)_x$ ( $x = 0.0$ – $0.4$ )
Base pressure	$1 \times 10^{-6}$ Torr	$1 \times 10^{-6}$ Torr	$1 \times 10^{-6}$ Torr
Gas used	High purity oxygen (99.7%)	High purity oxygen (99.7%)	High purity oxygen (99.7%)
Background oxygen pressure	10–100 mTorr	30 mTorr	30 mTorr
Substrate	Quartz	Quartz	Quartz
Substrate temperature	600 °C	600 °C	600 °C
Post annealing	–	600 °C for 30 min	–
Target to substrate distance	40 mm	40 mm	40 mm

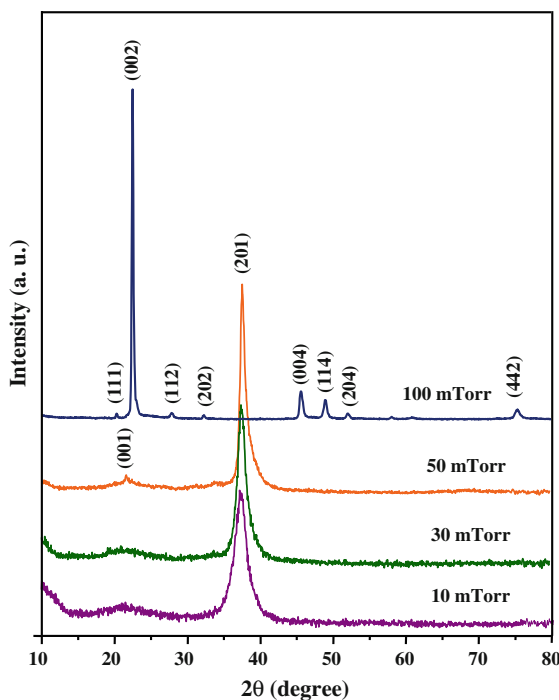


**Fig. 1** XRD pattern of  $\text{WO}_3$  thin films deposited at various oxygen partial pressures

the reactive scattering between evaporated materials and ambient oxygen gas molecules is significantly large thereby providing the oxide precursors required for the growth of films with the stoichiometric  $\text{WO}_3$  phase (Ohring 2002). The lattice parameters of these films were calculated using XRD data, which are listed in Table 2. The  $a$ -axis and  $c$ -axis length of the films deposited at 10, 30, and 50 mTorr were found to be 7.11, 4.01 Å; 7.16, 3.99; and 7.21, 3.94 Å, respectively, which were in close agreement with the lattice

parameters of bulk hexagonal  $\text{WO}_3$  ( $a = 7.298 \text{ \AA}$  and  $c = 3.899 \text{ \AA}$ ; JCPDS card No. 75-2187). Similarly,  $a$ ,  $b$  and  $c$ —the lattice parameters of the orthorhombic phase—were found to be 7.39, 7.63, and 7.76 Å, respectively, which were also in close agreement with the bulk orthorhombic phase of  $\text{WO}_3$  ( $a = 7.341 \text{ \AA}$ ,  $b = 7.570$ , and  $c = 7.754 \text{ \AA}$ ; JCPDS card No. 71-0131).

The crystallite size ( $d$ ) of these films was calculated using Scherrer's formula (Cullity and Stock 2001) given by

$$d_{hkl} = \frac{0.9\lambda}{\beta_{hkl} \cos \theta_{hkl}} \quad (1)$$

where  $\lambda$  is the X-ray wavelength,  $\beta_{hkl}$  is the full width at half maximum (FWHM) of the Bragg diffraction (in radians) on the  $2\theta$  scale, and  $\theta_{hkl}$  is the Bragg diffraction angle. Hussain et al. (2005) have reported a decrease in grain size from 206 nm to 90 nm for the  $\text{WO}_3$  films grown on Pyrex glass substrate with an increase in oxygen partial pressure from 100 to 300 mTorr. However in this study, the average grain size is found to increase from 13.2 nm to 24.8 nm with corresponding increase in oxygen partial pressure from 10 to 100 mTorr. The increase of crystallite size can be explained in terms of mean free path. In the presence of background oxygen gas, the molecular and atomic species in the ablated plume undergoes frequent collisions. As increase in oxygen partial pressure leads to decrease in mean free path, the number of collisions, undergone by molecular and atomic species in the plume with background oxygen atoms, increases. Owing to large number of collisions, the initially formed clusters have the tendency to coalesce with each other resulting in the formation of

**Table 2** Various calculated parameters of  $\text{WO}_3$  thin films of different oxygen partial pressure

Oxygen partial pressure (mTorr)	Crystallite size $d$ (nm) (from XRD)	Lattice parameters (Å)	Phase present	$E_g$ (eV)
10	13.2	$a = 7.11$ , $c = 4.01$	Hexagonal	3.32
30	16.5	$a = 7.16$ , $c = 3.99$	Hexagonal	3.39
50	19.8	$a = 7.21$ , $c = 3.94$	Hexagonal	3.48
100	24.8	$a = 7.39$ , $b = 7.63$ , $c = 7.76$	Orthorhombic	3.52

clusters of bigger size before deposition on the substrate.

Figure 2a shows the optical transmittance spectra of  $\text{WO}_3$  thin films deposited at different oxygen partial pressures of  $P_{\text{O}_2} = 10, 30, 50$ , and 100 mTorr. Optical transmittance of these films was found to increase with increase in oxygen partial pressure that could be because of the improvement in stoichiometry of the films. A similar trend of optical transmittance has also been reported by several research groups (Lethy et al. 2008; Gyorgy et al. 2005). A gradual shift of absorption edge toward a lower wavelength was observed with corresponding increase in oxygen partial pressure implying a blue shift in optical band gap. The indirect optical band gap of the film was calculated using the Tauc relationship (Tauc 1974) as follows:

$$\alpha h\nu = A(h\nu - E_g)^n \quad (2)$$

where  $\alpha$  is the absorption coefficient,  $A$  is a constant,  $h$  is the Planck's constant,  $\nu$  is the photon frequency,  $E_g$  is the energy band gap, and  $n$  is 2 for indirect band gap semiconductor. The indirect band gap of the  $\text{WO}_3$  film was evaluated by extrapolating the linear region of the curves  $(\alpha h\nu)^{1/2} = 0$  as shown in inset of Fig. 2b. The calculated values of the band gap ( $E_g$ ) were found to increase from 3.32, 3.39, 3.48 to 3.52 eV with increase in oxygen partial pressure from 10, 30, 50 to 100 mTorr, respectively (Table 2). The reason of increase in bandgap could be attributed to the fact that increased oxygen partial pressure leads to reduction of oxygen vacancies, which is correlated with the formation of deep localized states in the bandgap.

#### Effect of post annealing on optical properties of $\text{WO}_3$ thin films

In order to study the annealing effect, the  $\text{WO}_3$  films deposited at substrate temperature of 600 °C and oxygen partial pressure of 30 mTorr were post annealed in vacuum for 30 min at the same temperature and compared with as-deposited film. Optical transmittance of as-deposited film was found to be higher as compared to the annealed  $\text{WO}_3$  films as shown in Fig. 3a. It was observed that the film color changed from transparent to a deep shade of blue color. The origin of this blue color is the presence of oxygen vacancies (i.e.  $\text{WO}_{3-y}$ ) associated with

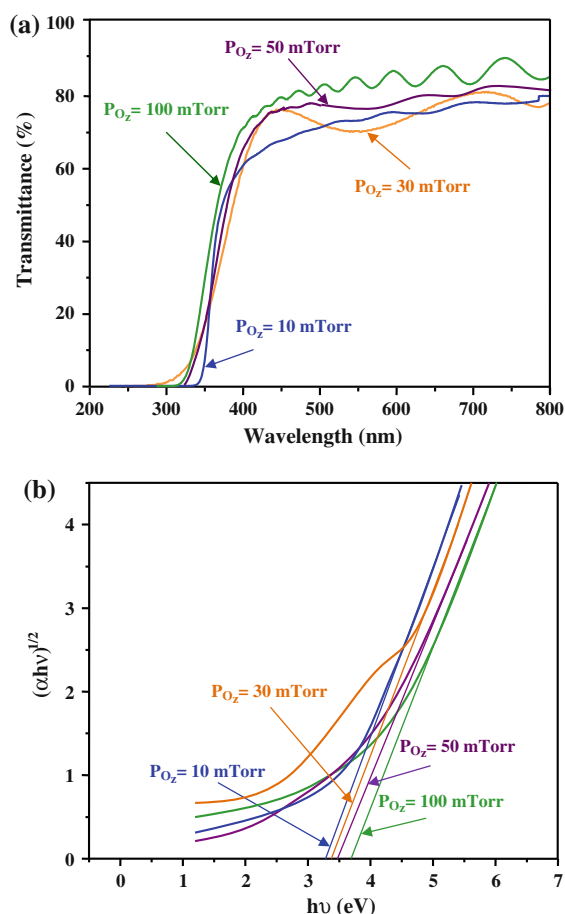


**Fig. 2** **a** Transmission spectra and **b**  $(\alpha h\nu)^{1/2}$  versus  $h\nu$  plot for band gap calculation of  $\text{WO}_3$  thin films deposited at different oxygen partial pressures ( $P_{\text{O}_2}$ )

tungsten ions in lower oxidation states than the 6+ expected in  $\text{WO}_3$  stoichiometry. The creation of oxygen vacancies can be expressed by the chemical equilibrium as follows (Gillet et al. 2003):



where  $\text{O}_0^X$  represents the neutral oxygen atom in an oxide site, and  $\text{V}_0^X$  represents the neutral oxygen vacancy with two trapped electrons. The indirect optical band gap (Fig. 3b) of the films was calculated using the Tauc relationship, which was found to decrease from 3.39 to 3.15 eV with vacuum annealing, which could be because of the increase of oxygen vacancies. A similar trend in optical band gap with change in annealing temperature has also been recently reported by Gondal et al. (2009, 2010) in

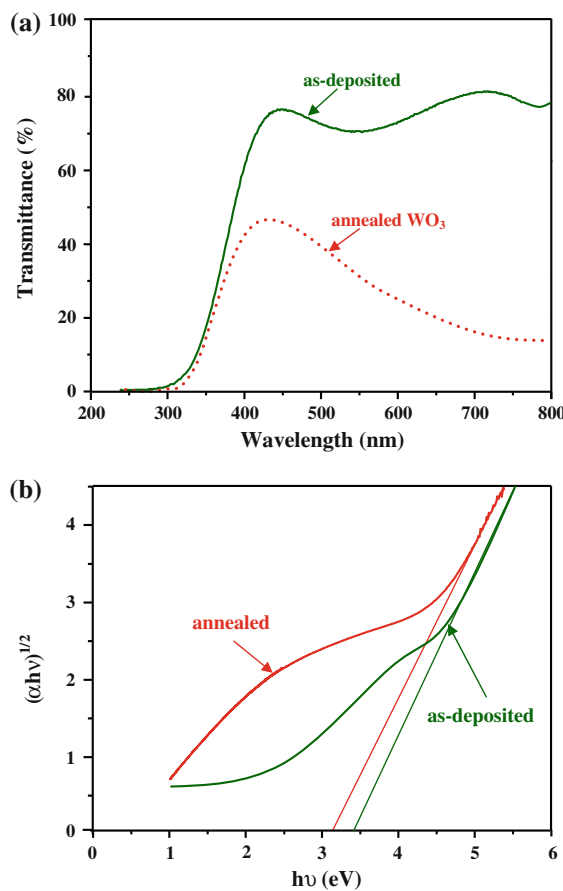


**Fig. 3** **a** Transmission spectra and **b**  $(\alpha h\nu)^{1/2}$  versus  $h\nu$  plot of the as-deposited and annealed  $\text{WO}_3$  thin film

case of  $\text{ZnO}$  and  $\text{SnO}_2$  nanoparticles synthesized by PLD.

#### Effect of $\text{VO}_2$ content on structural, optical, and electrochemical properties of $(\text{WO}_3)_{1-x}(\text{VO}_2)_x$ thin films

Our main focus in this section will be to examine the effect of  $\text{VO}_2$  doping on structural, optical, and electrochemical properties of hexagonal  $\text{WO}_3$  ( $h\text{-WO}_3$ ) thin films. The hexagonal form of  $\text{WO}_3$  was chosen because of its well-known tunnel structure that has attracted much interest, and thus, being widely investigated as an intercalation host for obtaining hexagonal tungsten bronzes  $M_x\text{WO}_3$  ( $M = \text{Li}^+, \text{Na}^+, \text{K}^+, \text{H}^+$ , etc.). Figure 4 shows the XRD pattern of  $(\text{WO}_3)_{1-x}(\text{VO}_2)_x$  thin films of different  $\text{VO}_2$  contents ranging from  $x = 0.0, 0.1, 0.2, 0.3$  to  $0.4$ . It was observed that  $h\text{-WO}_3$  film

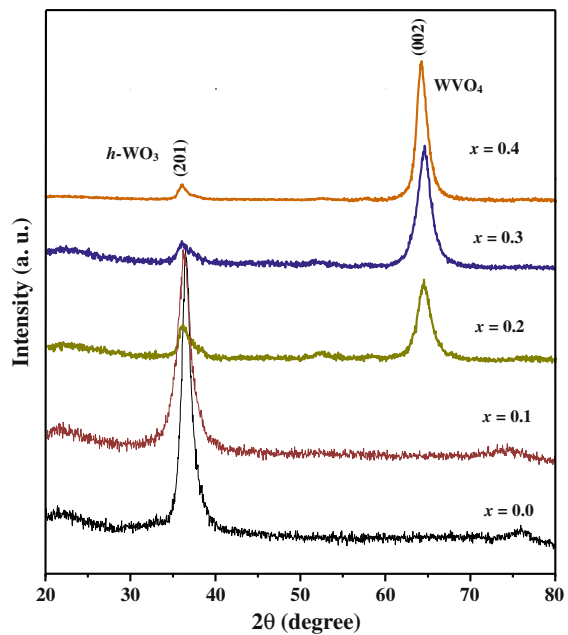


**Fig. 4** XRD pattern of  $(\text{WO}_3)_{1-x}(\text{VO}_2)_x$  thin films for different  $x = 0.0, 0.1, 0.2, 0.3$  and  $0.4$

doped with low  $\text{VO}_2$  content of  $x = 0.1$  exhibited highly oriented (201) diffraction peak with a slight shift toward lower  $2\theta$  value, which revealed the substitution of vanadium ions in  $\text{WO}_3$ . Further increase in  $\text{VO}_2$  content to  $x = 0.2, 0.3$ , and  $0.4$  leads to the formation of additional  $\text{WVO}_4$  phase with dominant (002) diffraction peak along with (201) peak of  $h\text{-WO}_3$  phase (indexed from JCPDS card No. 38-0012). The presence of  $\text{WVO}_4$  phase along with pure  $\text{WO}_3$  phase at  $x = 0.2, 0.3$  and  $0.4$  in XRD spectra shows a segregation of the W–V–O composite. The crystallite size of these films was calculated along (201)  $h\text{-WO}_3$  phase using Scherrer's formula and was found to be decreasing from 16.5 nm, 14.46, 13.73, 12.65 to 11.86 with increasing  $\text{VO}_2$  content from  $x = 0.0, 0.1, 0.2, 0.3$ , to  $0.4$ , respectively (Table 3). The decrease in crystallite size could be due to the structural adjustment of  $h\text{-WO}_3$  with the substitution of vanadium as the ionic radius of  $\text{W}^{6+}$  (0.64 Å) is larger than that of ionic radius of  $\text{V}^{4+}$  (0.63 Å). The presence of V in the  $\text{WO}_3$  thin films was confirmed by EDAX measurement. Figure 5 shows the EDAX spectra for the films with  $x = 0.1$ . EDAX pattern gives values of 79.56 and 8.87 wt% of W and V element, respectively, which shows an evidence of the presence of both W as well as V in

**Table 3** Various parameters of  $\text{VO}_2\text{-WO}_3$  thin films of different  $\text{VO}_2$  content

$\text{VO}_2$ content	Crystallite size (nm)		Lattice parameters ( $\text{\AA}$ )	$E_g$ (eV)	Phase present
	XRD	AFM			
$x = 0$	16.5	55	$a = 7.163,$ $c = 3.991$	3.39	$h\text{-WO}_3$
$x = 0.1$	14.46	45	$a = 7.147,$ $c = 3.954$	2.96	$h\text{-WO}_3$
$x = 0.2$	13.73	36	$a = 7.135,$ $c = 3.927$	2.89	$h\text{-WO}_3 + \text{WVO}_4$
$x = 0.3$	12.65	29	$a = 7.128,$ $c = 3.913$	2.78	$h\text{-WO}_3 + \text{WVO}_4$
$x = 0.4$	11.86	26	$a = 7.119,$ $c = 3.906$	2.61	$h\text{-WO}_3 + \text{WVO}_4$

the composite. The spectra show somewhat smaller value of the W:V ratio than the ratio present in the targets. This could be attributed to the different ablation mechanism of tungsten and vanadium oxides during the thin films growth.

Figure 6a–e shows the AFM micrographs of  $(\text{WO}_3)_{1-x}(\text{VO}_2)_x$  films corresponding to various values of  $x$  from 0.0 to 0.4. The average grain size calculated from these micrographs follows the same trend as observed in case of crystallite size calculated from XRD data and is found to decrease with increase in  $\text{VO}_2$  content (Table 3). Figure 7a and b depicts a histogram showing grain size distribution and plots for crystallite size (calculated from Eq. 1) and grain size (observed from AFM images) variations with different values of  $x$ . It has been found that the grain size obtained from AFM is larger by about a factor of 4 compared to that determined from XRD results. This difference is mainly caused by the different grain size criteria underlying the different methods. The AFM grain sizes are measured by the distances between the visible grain boundaries, whereas the XRD methods determines the extension of the crystalline that diffract the X-rays coherently, which is more stringent criteria, thus leading to smaller size. It can also be clearly seen that the density of grains increases with increase in  $\text{VO}_2$  content.

Figure 8a shows the optical transmittance spectra of these films. A systematic decrease in percentage of transmission was observed with increase in  $\text{VO}_2$  content, which could be because of the enhancement of (a) light absorption by increase of  $\text{W}^{5+}/\text{W}^{6+}$  ratio and (b) light scattering by increase of grain density

(Ranjbar et al. 2008). Indirect optical band gap (Fig. 8b) of these films calculated from transmission spectra was found to decrease from 3.39 eV ( $x = 0.0$ ), to 2.96 eV ( $x = 0.1$ ), 2.89 eV ( $x = 0.2$ ), 2.78 eV ( $x = 0.3$ ), and to 2.61 eV ( $x = 0.4$ ) (Table 3). The reason for the red shift in optical band gap could be attributed to the fact that the substitution of vanadium with tungsten ions exhibited a lower oxidation state, which is associated with the oxygen vacancies. Therefore, an increase in vanadium content is correlated to the increase in oxygen vacancy that creates donor levels below the conduction band of  $\text{WO}_3$  leading to a progressive overlap and decrease in band gap.

The refractive index ( $n$ ) was estimated from the transmission spectrum using the envelope method, and the following expression was used to calculate the refractive index:

$$n = \left[ N + (N^2 - n_0^2 n_1^2)^{1/2} \right]^{1/2}, \quad (4)$$

where

$$N = \frac{n_0^2 + n_1^2}{2} + 2n_0 n_1 \frac{T_{\max} - T_{\min}}{T_{\max} T_{\min}} \quad (5)$$

and  $n_0$  and  $n_1$  (1.46 in our case) are the refractive indices of air and substrate, respectively.  $T_{\max}$  and  $T_{\min}$  are the corresponding maximum and minimum transmittance values at the same wavelength. Figure 9 represents the refractive indices ( $n$ ) calculated at different wavelengths for deposited thin films of different  $x$ . The average value of refractive indices ( $n$ ) evaluated at different wavelengths was found to

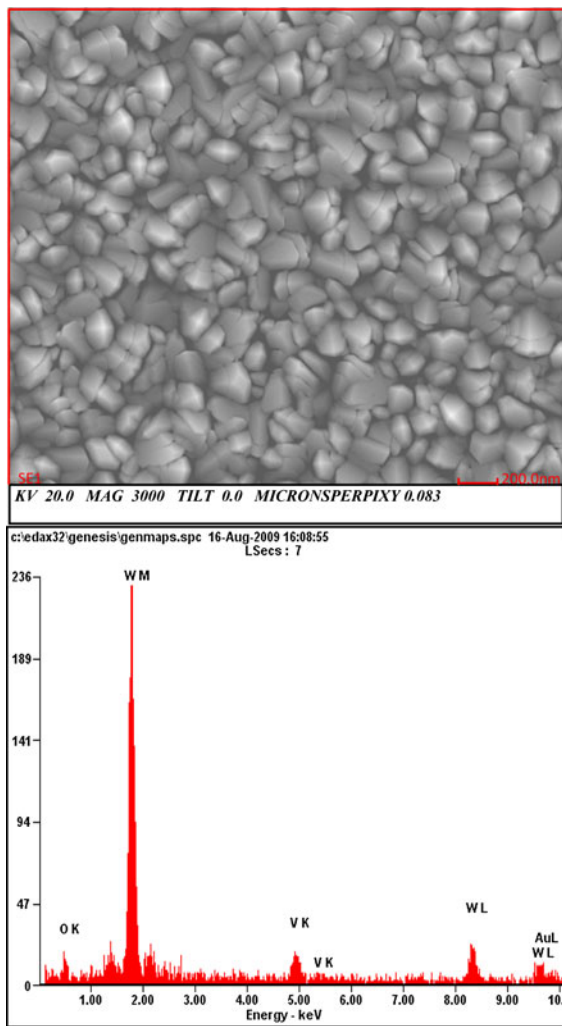


**Fig. 5** EDAX spectra for film with  $x = 0.1$

increase with increase in  $x$ . Figure 10a shows the variation of refractive index ( $n$ ) (at fixed wavelength of 550 nm) and optical band gap for films with different values of  $x$ . The calculated values of refractive index were found to be 1.90 ( $x = 0.0$ ); 1.93 ( $x = 0.1$ ); 1.96 ( $x = 0.2$ ); 2.0 ( $x = 0.3$ ); and 2.03 ( $x = 0.4$ ). In general, the refractive indices of the oxides can be related to the dispersion energy parameters  $E_d$  and  $E_0$ , using the single term Sellmeier dispersion relation (Didomenico and Wemple 1969; Wemple and Didomenico 1971):

$$n^2 = 1 + \frac{E_d E_0}{(E_0^2 - h^2 v^2)} \quad (6)$$

where,  $h\nu$  is the photon energy, and  $E_0$  is the single oscillator energy. The parameter  $E_d$  is the dispersion

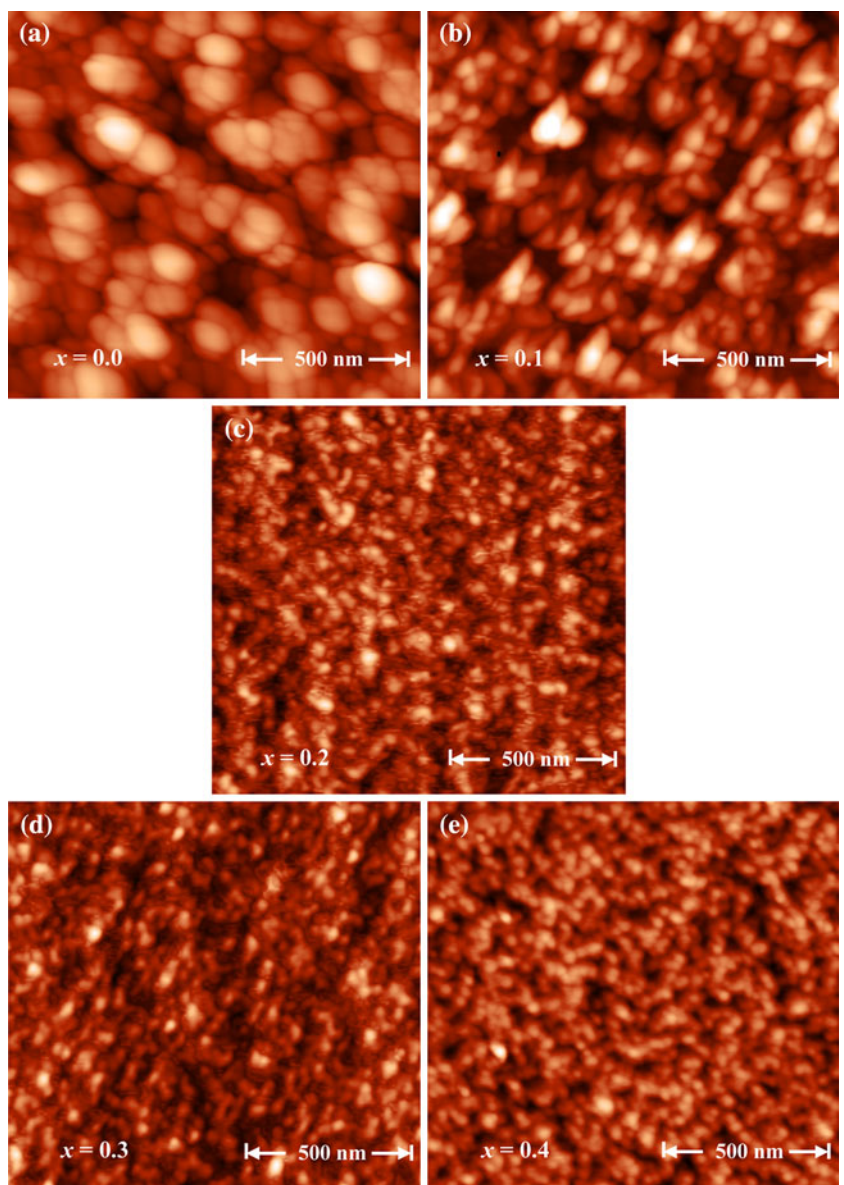
energy, which is a measure of the strength of interband optical transitions. The optical band gap value can be derived from Wemple–Didomenico dispersion parameters using the relation  $E_g \approx E_0/2$  (Marquez et al. 1999), which is directly proportional to refractive index ( $n$ ). The strength of interband transitions depends on the mass density and the degree of the packing density in the interfaces (Benthem et al. 2004, 2006). The possible reasons for the variation of refractive index are a variation of binding states of  $\text{WO}_3$  due to oxygen vacancies which causes an alteration of the single oscillator energy in Wemple–Didomenico model and secondly, a possible variation of the packing density (Ito and Nakzaewa 1983). AFM images of deposited films shows an increase of packing density and physical density with increase in  $\text{VO}_2$  content which results in corresponding increase in refractive index. The film porosity is directly related to the index of refraction by the expression

$$p = \left(1 - \frac{n_{\text{film}}}{n_{\text{bulk}}}\right) \quad (7)$$

where  $n_{\text{film}}$  is the index of refraction measured for films, and  $n_{\text{bulk}}$  is the index of refraction for bulk  $\text{WO}_3$ . From the expression, an increase in index of refraction of the films translates to a decrease in porosity of the films which can be clearly seen from the AFM images with increase in  $\text{VO}_2$  content. Variations of refractive index ( $n$ ) and optical band gap ( $E_g$ ) with grain size have also been plotted in Fig. 10b which show a decrease of refractive index with increase in grain size.

Figure 11 shows the cyclic voltammogram of the as-deposited  $(\text{WO}_3)_{1-x}(\text{VO}_2)_x$  thin films of different  $\text{VO}_2$  contents ranging from  $x = 0.0$  to  $x = 0.4$  at a scan rate of  $100 \text{ mVs}^{-1}$  between initial and final switching potentials of  $+1000$  and  $-1000 \text{ mV}$ , respectively. As the potential varied from  $+1000$  to  $-1000 \text{ mV}$ , the film electrodes with  $x = 0.0$  and  $0.1$  show the current density as being close to zero until the potential drops below 0 at which the current density becomes progressively negative. This branch corresponds to intercalation, where ions from the electrolyte are coinserted into the  $\text{WO}_3$  films. This progressive increase in the cathodic current indicates the reduction of the  $\text{W}^{6+}$  ionic state to  $\text{W}^{5+}$  state (Rougier et al. 2002). The following one-electron process occurs as follows (Hersh et al. 1975):

**Fig. 6** AFM images of  $(\text{WO}_3)_{1-x}(\text{VO}_2)_x$  thin films of different  $\text{VO}_2$  contents  
**a**  $x = 0.0$ , **b**  $x = 0.1$ ,  
**c**  $x = 0.2$ , **d**  $x = 0.3$ , and  
**e**  $x = 0.4$



As the current density changes from negative values, after reversing the scan direction at  $-1000$  mV, deintercalation starts. The deintercalation current passes through a maximum and finally becomes approximately zero at potential beyond  $0$  mV. With increase in  $\text{VO}_2$  content to  $x = 0.2$ ,  $0.3$ , and  $0.4$ , a modification has been observed in the shape of the cyclic voltammogram in the form of the appearance of an extra cathodic peak at  $-300$ ,  $-450$ , and  $-650$  mV, respectively. The intensity of the peak

increases with increase in  $\text{VO}_2$  content. The observed cathodic peak may be attributed to the reduction of  $\text{WVO}_4$  phase as depicted from XRD results. The behavior of cyclic voltammogram is in consistence with reported results. They attributed this peak to  $\text{V}^{+5}$  reductions. Moreover, as the  $\text{VO}_2$  increases, the film electrodes show a poor deintercalation capacity as anodic peak intensity decreases. The absence of any extra cathodic peak in case of  $10\%$   $\text{VO}_2$  electrodes indicates that the electrochemical behavior of these electrodes cannot be described as simultaneous behavior of individual  $\text{WO}_3$  and  $\text{VO}_2$ , favoring the

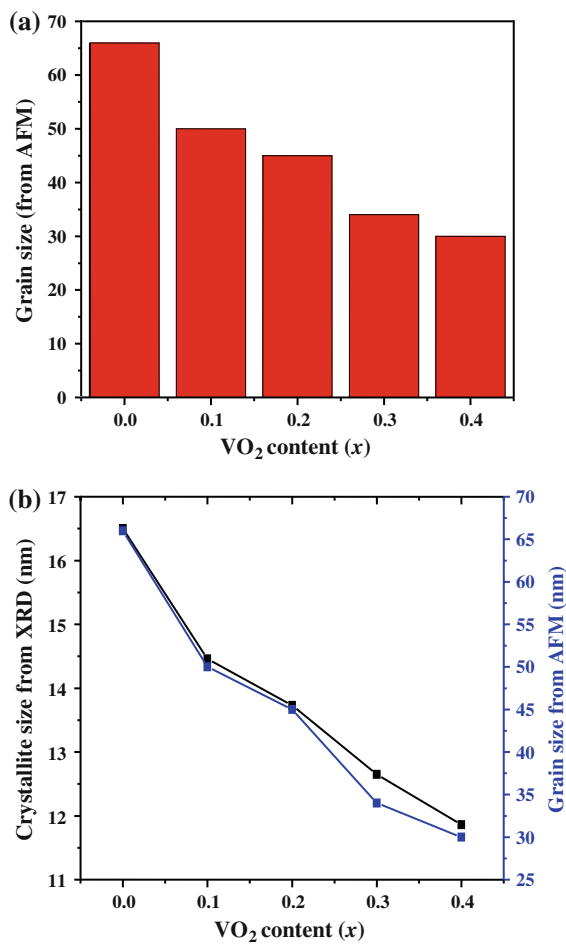


**Fig. 7** **a** Histogram showing grain size distribution and **b** plots for crystallite and grain size variations with different values of  $x$

solid solubility limit of  $\text{VO}_2$  in  $\text{WO}_3$ , which is in agreement with the XRD results obtained.

## Conclusion

In summary, the effects of oxygen partial pressure, post-annealing and  $\text{VO}_2$  content on various properties of nanocrystalline  $\text{WO}_3$  thin films have been systematically investigated. XRD studies reveal the hexagonal phase for  $\text{WO}_3$  thin films deposited at 600 °C with lower oxygen partial pressure of 10, 30, and 50 mTorr. An increase in oxygen partial pressure leads to increase of crystallite size and optical transmittance of these films. In situ vacuum annealing of

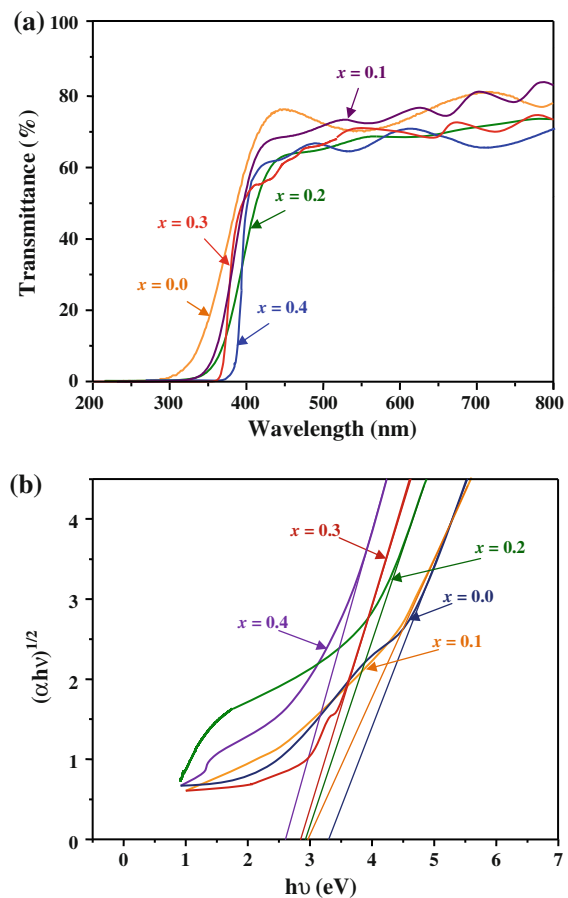


**Fig. 8** **a** Transmission spectra and **b**  $(\alpha h\nu)^{1/2}$  versus  $h\nu$  plot for indirect band gap calculation of  $(\text{WO}_3)_{1-x}(\text{VO}_2)_x$  thin films of different  $\text{VO}_2$  contents ( $x$ )

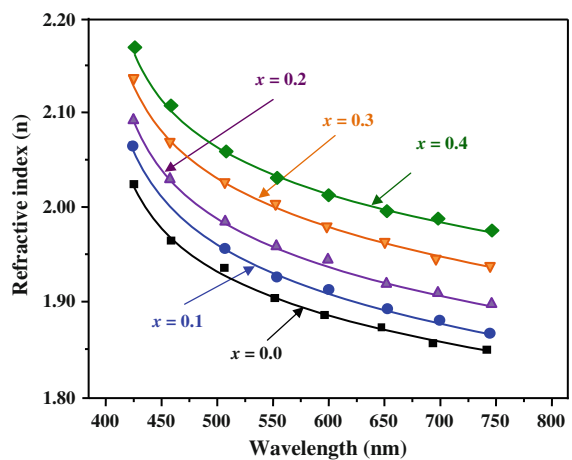


**Fig. 9** Refractive index values of  $(\text{WO}_3)_{1-x}(\text{VO}_2)_x$  thin films of different  $\text{VO}_2$  contents ( $x$ )

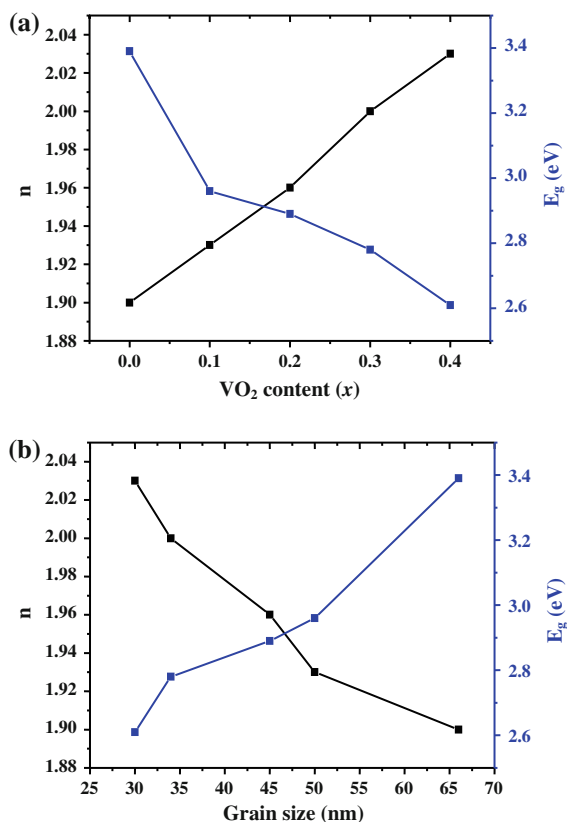


**Fig. 10** Variation of refractive index ( $n$ ), optical band gap for films with different values of **a**  $x$  and **b** grain sizes

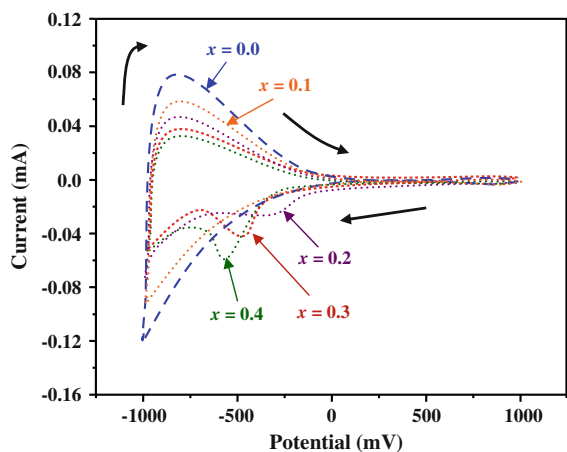


**Fig. 11** CV characteristics of  $(\text{WO}_3)_{1-x}(\text{VO}_2)_x$  thin films of different  $\text{VO}_2$  content ( $x$ )

$\text{WO}_3$  thin film changed the color from transparent as-deposited to deep shade of blue color which increases the optical absorption of the film. The origin of this blue color could be due to the presence of oxygen

vacancies associated with tungsten ions in lower oxidation states. Increase in  $\text{VO}_2$  content ( $x \geq 0.2$ ) in  $(\text{WO}_3)_{1-x}(\text{VO}_2)_x$  films exhibited the formation of  $\text{WVO}_4$  phase as revealed by XRD pattern. Red shift in optical band gap was observed that could be because of an increase in vanadium content and was correlated to the oxygen vacancies. The average value of refractive indices ( $n$ ) was found to increase from 1.90 to 2.03 with corresponding increase in  $\text{VO}_2$  content ranging from  $x = 0.0$  to 0.4. Cyclic voltammogram exhibited a modification with the appearance of an extra cathodic peak with increase in vanadium content. The absence of any extra cathodic peak in the case of 10%  $\text{VO}_2$  electrodes favors the solid solubility limit of  $\text{VO}_2$  in  $\text{WO}_3$  in agreement to XRD results.

**Acknowledgments** The financial support provided by the Ministry of Communications and Information Technology (MIT), India under the Nanotechnology Initiative Program, Reference no. 20(11)/2007-VCND and Armament Research Board (ARMREB), DRDO New Delhi with reference number ARMREB/MAA/2008/91, is highly acknowledged.

## References

- Ashokkumar M, Maruthamuthu P (1989) Factors influencing the photocatalytic efficiency of  $\text{WO}_3$  particles. *J Photochem Photobiol A Chem* 49:249–258
- Benthem KV, Tan G, Linda K, Noyer D, French RH, Ruhle M (2004) Local optical properties, electron densities, and London dispersion energies of atomically structured grain boundaries. *Phys Rev Lett* 93:227201–227204
- Benthem KV, Tan G, French RH, Linda K, Noyer D, Podgornik R, Parsegian VA (2006) Graded interface models for more accurate determination of van der Waals—London dispersion interactions across grain boundaries. *Phys Rev B* 74:205110–205121
- Christian GD, Purdy WC (1982) The residual current in orthophosphate medium. *J Electroanal Chem* 3:363–367
- Cullity BD, Stock SR (2001) Elements of X-Ray diffraction, 3rd edn. Prentice Hall, Upper Saddle River, NJ
- Didomenico M, Wemple SH (1969) Oxygen-octahedra ferroelectrics. I. Theory of electro-optical and nonlinear optical effects. *J Appl Phys* 40:720–734
- Mitsugi F, Hiraiwa E, Ikegami T, Ebihara K (2003) Pulsed laser deposited  $\text{WO}_3$  thin films for gas sensor. *Surf Coat Technol* 169:553–556
- Gerand B, Nowogrocki G, Guenot J, Figlarz M (1979) Structural study of a new hexagonal form of tungsten trioxide. *J Solid State Chem* 29:429–434
- Gillet M, Lemire C, Gillet E, Aguir K (2003) The role of surface oxygen vacancies upon  $\text{WO}_3$  conductivity. *Surf Sci* 532:519–525
- Gondal MA, Drmosh QA, Yamani ZH, Saleh TA (2009) Synthesis of  $\text{ZnO}_2$  nanoparticles by laser ablation in liquid

- and their annealing transformation into ZnO nanoparticles. *Appl Surf Sci* 256:298–304
- Gondal MA, Drmosh QA, Saleh TA (2010) Preparation and characterization of SnO<sub>2</sub> nanoparticles using high power pulsed laser. *Appl Surf Sci* 256:7067–7070
- Granqvist CG (1990) Window coatings for the future. *Thin Solid Films* 193:730–741
- Granqvist CG (1991) Energy-efficient windows: present and forthcoming technology in Material Science for Solar Energy Conversion Systems. Pergamon, Oxford, Chp. 5
- Granqvist CG, Avendano E, Azens A (2003) Electrochromic coatings and devices: survey of some recent advances. *Thin Solid Films* 442:201–211
- Gyorgy E, Socol G, Mihailescu IN, Ducu C, Ciucă S (2005) Structural and optical characterization of WO<sub>3</sub> thin films for gas sensor applications. *J Appl Phys* 97:093527–093530
- Hersh HN, Kramer WE, McGee JH (1975) Mechanism of electrochromism in WO<sub>3</sub>. *Appl Phys Lett* 27:646–648
- Hussain OM, Swapnasmita AS, John J, Pinto R (2005) Structure and morphology of laser-ablated WO<sub>3</sub> thin films. *Appl Phys A* 81:1291–1297
- Ingham B, Hendy SC, Chong SV, Tallon JL (2005) Density-functional studies of tungsten trioxide, tungsten bronzes, and related systems. *Phys Rev B* 72:075109–075117
- Ito K, Nakzaewa T (1983) Transparent and highly conductive films of ZnO prepared by RF sputtering. *Jpn J Appl Phys* 22:L245–L247
- Jelle BP, Hagen G (1999) Performance of an electrochromic window based on polyaniline, Prussian blue and tungsten oxide. *Sol Energy Mater Sol Cells* 58:277–286
- Kaneko H, Nagao F, Miyake K (1988) Preparation and properties of the dc reactively sputtered tungsten oxide films. *J Appl Phys* 63:510–517
- Kaur D, Jesudasan J, Raychaudhuri P (2005) Pulsed laser deposition of NdNiO<sub>3</sub> thin films. *Solid State Commun* 136:369–374
- Kumagai N, Kumagai N, Umetzu Y, Tanno K, Pereira-Ramos JP (1996) Synthesis of hexagonal form of tungsten trioxide and electrochemical lithium insertion into the trioxide. *Solid State Ionics* 86:1443–1449
- Kumar A, Singh P, Kaur D, Jesudasan J, Raychaudhuri P (2006) Substrate effect on electrical transport properties of RNiO<sub>3</sub> thin films prepared by pulsed laser deposition. *J Phys D Appl Phys* 39:5310–5315
- Lee KH, Fang YK, Lee WJ, Ho JJ, Chen KH, Liao KS (2000) Novel electrochromic devices (ECD) of tungsten oxide (WO<sub>3</sub>) thin film integrated with amorphous silicon germanium photodetector for hydrogen sensor. *Sens Actuators B* 69:96–99
- Lethy KJ, Beena D, Kumar RV, Pillai VPM, Ganeshan V, Sathe V, Phase DM (2008) Nanostructured tungsten oxide thin films by the reactive pulsed laser deposition technique. *Appl Phys A* 91:637–649
- Marquez E, Bernal-Oliva AM, Gonzalez-Leal JM, Pricto-Alcon R, Ledesma A, Jimenez-Garay R, Martil I (1999) Optical-constant calculation of non-uniform thickness thin films of the Ge10As15Se75 chalcogenide glassy alloy in the sub-band-gap region (0.1–1.8 eV). *Mater Chem Phys* 60:231–239
- Ohring M (2002) Material science of thin films. Academic Press, San Diego
- Ozer N, Lampert CM (1998) Electrochromic characterization of sol-gel deposited coatings. *Sol Energy Mater Sol Cells* 54:147–156
- Pecquenard B, Lecacheux H, Livage J, Julien C (1998) Orthorhombic WO<sub>3</sub> formed via a Ti-Stabilized WO<sub>3</sub> $\frac{1}{3}$ H<sub>2</sub>O Phase. *J Solid State Chem* 135:159–168
- Pickering R, Tilley RJD (1976) An electron microscope study of tungsten oxides in the composition range WO<sub>2.90</sub>–2.72. *J Solid State Chem* 16:247–255
- Poirier G, Cassanjes FC, Messadeq Y, Ribeiro SJL (2009) Crystallization of monoclinic WO<sub>3</sub> in tungstate fluorophosphate glasses. *J Non-Cryst Solids* 355:441–446
- Qu WM, Włodarski W (2000) A thin-film sensing element for ozone, humidity and temperature. *Sens Actuators B* 64: 42–48
- Ranjbar M, Mahdavi SM, Iraji zad A (2008) Pulsed laser deposition of W-V-O composite films: Preparation, characterization and gasochromic studies. *Sol Energy Mater Sol Cells* 92:878–883
- Regragui M, Joussemae V, Addou M, Outzourhit A, Bernede JC, El Idrissi B (2001) Electrical and optical properties of WO<sub>3</sub> thin films. *Thin Solid Films* 397:238–243
- Robert GP, Ivan PP (2004) Aerosol assisted chemical vapour deposition of photochromic tungsten oxide and doped tungsten oxide thin films. *J Mater Chem* 14:2864–2867
- Rougier A, Quedé A (2001) Electrochromism of mixed tungsten-vanadium oxide thin films grown by pulsed laser deposition. *J Electrochem Soc* 148:H7–H12
- Rougier A, Portemer F, Quedé A, Marssi ME (1999) Characterization of pulsed laser deposited WO<sub>3</sub> thin films for electrochromic devices. *Appl Surf Sci* 153:1–9
- Rougier A, Blyr A, Garcia J, Zhang Q, Impey SA (2002) Electrochromic W-M-O (M=V, Nb) sol-gel thin films: a way to neutral colour. *Sol Energy Mater Sol Cells* 71: 343–357
- Sivakumar R, Gopalakrishnan R, Jayachandran M, Sanjeevi-raja C (2007) Preparation and characterization of electron beam evaporated WO<sub>3</sub> thin films. *Opt Mat* 29:679–687
- Takami H, Kanki T, Ueda S, Kobayashi K, Tanaka H (2010) Electronic structure of W-doped VO<sub>2</sub> thin films with giant metal-insulator transition investigated by hard X-ray core-level photoemission spectroscopy. *Appl Phys Express* 3: 063201–063203
- Tauc J (1974) Amorphous and liquid semiconductor. Plenum Press, New York
- Walkingshaw AD, Spaldin NA, Artacho E (2004) Density-functional study of charge doping in WO<sub>3</sub>. *Phys Rev B* 70:165110–165116
- Wemple SH, Didomenico M (1971) Behavior of the electronic dielectric constant in covalent and ionic materials. *Phys Rev B* 3:1338–1351